https://doi.org/10.5194/acp-2021-463
Preprint. Discussion started: 22 June 2021

Atmospheric Chemistry and Physics Discussions

Bimodal distribution of size-resolved particle effective density in a rural environment in the North China Plain

Yaqing Zhou[1,2], Nan Ma[1,2], Qiaoqiao Wang[1,2], Zhibin Wang[3], Chunrong Chen[4], Jiangchuan Tao[1,2], Juan Hong[1,2], Long Peng[1,2], Yao He[1,2], Linhong Xie[1,2], Shaowen Zhu[1,2], Yuxuan Zhang[5,6], Guo Li[5], Wanyun Xu[7], Peng Cheng[8], Uwe Kuhn[5], Guangsheng Zhou[7], Pingqing Fu[9], Qiang Zhang[4], Hang Su[5], Yafang Cheng[5]

[1]Institute for Environmental and Climate Research, Jinan University, Guangzhou, 511443, China
[2]Guangdong-Hongkong-Macau Joint Laboratory of Collaborative Innovation for Environmental Quality, Guangzhou, 511443, China
[3]Research Center for Air Pollution and Health, College of Environmental and Resource Sciences, Zhejiang University, Hangzhou, 310058, China
[4]Department of Earth System Science, Tsinghua University, Beijing, 100084, China
[5]Multiphase Chemistry Department, Max Planck Institute for Chemistry, Mainz, 55128, Germany
[6]School of Atmospheric Sciences, Nanjing University, Nanjing, 210093, China
[7]State Key Laboratory of Severe Weather, Key Laboratory for Atmospheric Chemistry, Institute of Atmospheric Composition and Environmental Meteorology, Chinese Academy of Meteorological Sciences, Beijing, 100081, China
[8]Institute of Mass Spectrometry and Atmospheric Environment, Jinan University, Guangzhou, 510632, China
[9]Institute of Surface-Earth System Science, Tianjin University, Tianjin, 300072, China
Correspondence to: Nan Ma (nan.ma@jnu.edu.cn) and Qiaoqiao Wang (q.wang2@outlook.com)

Abstract. Effective density is one of the most important physical properties of atmospheric particles. It is closely linked to particle chemical composition and morphology, and could provide special information on particle emissions and aging processes. In this study, size-resolved particle effective density was measured with a combined DMA-CPMA-CPC system in Multiphase chemistry experiment in Fogs and Aerosols in the North China Plain (McFAN) in autumn 2019. With a new developed flexible Gaussian fit algorithm, frequent (77 %-87 %) bimodal distribution of particle effective density is identified, with a low-density mode (named sub-density mode) accounting for 22 %-27 % of total observed particles. The prevalence of the sub-density mode is closely related to fresh black carbon (BC) emissions. The geometric mean for the main-density mode ($\bar{\rho}_{\mathrm{eff,main}}$) increases from 1.18 g cm^{-3} (50 nm) to 1.37 g cm^{-3} (300 nm) due to larger fraction of high-density components and more significant restructuring effect at large particle sizes, but decreases from 0.89 g cm^{-3} (50 nm) to 0.62 g cm^{-3} (300 nm) for the sub-density mode ($\bar{\rho}_{\mathrm{eff,sub}}$) ascribed to the agglomerate effect. $\bar{\rho}_{\mathrm{eff,main}}$ and $\bar{\rho}_{\mathrm{eff,sub}}$ show similar diurnal cycles with peaks in the early afternoon, mainly attributed to the increasing mass fraction of high material density components associated with secondary aerosol production, especially of secondary inorganic aerosol (SIA). To investigate the impact of chemical composition, bulk particle effective density was calculated based on measured chemical composition ($\rho_{\mathrm{eff,ACSM}}$) and compared with the average effective density at 300 nm ($\bar{\rho}_{\mathrm{eff,tot,300nm}}$). The best agreement between the two densities is achieved when assuming a BC effective density of 0.60 g cm^{-3}. The particle effective density is highly dependent on SIA and BC mass fractions. The influence of BC on the effective density is even stronger than SIA, implying the importance and necessity of including BC in the estimate of effective density for ambient particles.

https://doi.org/10.5194/acp-2021-463
Preprint. Discussion started: 22 June 2021


Atmospheric Chemistry and Physics Discussions

1 Introduction

Atmospheric aerosol has a significant impact on air quality, climate change and public health (Dockery and Pope, 1994; IPCC, 2007; Laden et al., 2000; Su et al., 2020). This is determined by a combination of various particle physical and chemical properties. Density, as one of important physical properties of aerosol particles, is intimately associated with particles' optical, chemical and dynamic properties (Ditas et al., 2018; Nosko and Olofsson, 2017; Park et al., 2003). It serves as a link between particle mass and mobility size (McMurry et al., 2002; Schmid et al., 2007), and is usually used to infer particle morphology, chemical composition, and associated atmospheric processes such as emission and aging (Abegglen et al., 2015; Levy et al., 2013; Olfert et al., 2007; Olfert et al., 2017; Park et al., 2003; Wang et al., 2018; Wu et al., 2019; Zhang et al., 2018). Owing to the inability to directly measure the density of atmospheric particles, effective density is usually applied practically in aerosol research.

The effective density is closely linked to particle chemical composition and morphology. It is generally observed within the range of 1.06-1.81 g cm^{-3} in the ambient atmosphere (Cha and Olofsson, 2018; Geller et al., 2006; Hu et al., 2012; Levy et al., 2014; Lin et al., 2018; Rissler et al., 2014; Zamora et al., 2019), of which high values are attributed to the dominant of ammonium sulfate ($(NH_4)_2SO_4$), ammonium nitrate (NH_4NO_3) and metals (Zhai et al., 2017; Zhang et al., 2016a). In contrast, the effective density of black carbon (BC) or organic aerosol (OA) dominated particles is relatively low (Zhai et al., 2017). While the effective densities of inorganic components are well recognized, there exits large uncertainties in the effective densities of both BC and OA (Li et al., 2016; Malloy et al., 2009; Zhang et al., 2008), leading to significant variations in the effective densities of ambient bulk particles.

The variability of OA density primarily originates from the diversity of organic species, formation mechanisms and aging processes. For instance, the effective density of secondary organic aerosol (SOA) oxidated from *m*-xylene, terpenes and cycloalkenes was estimated to be around 1.10 g cm^{-3} for those generated with inorganic seeds but around 1.40 g cm^{-3} without seeds (Bahreini et al., 2005). Malloy et al., (2009) determined effective densities of 1.24 g cm^{-3} and 1.35 g cm^{-3} for SOA from ozonolysis of α-pinene and photo-oxidation of *m*-xylene, respectively. An increase of 10 % in effective density caused by oxidative aging process was also observed for SOA (George and Abbatt, 2010). Little information is found for effective density of primary organic aerosol (POA), but its value is usually lower than that of SOA due to closely related to fresh emissions (Nakao et al., 2011). Generally, a simplified average value around 1.20-1.40 g cm^{-3} is commonly applied for ambient OA in numerous studies (e.g. Hallquist et al., 2009; Hu et al., 2012; Levy et al., 2013).

A more dramatic variation is observed for the effective density of BC, ranging from 0.10 to 1.80 g cm^{-3} (Pagels et al., 2009; Peng et al., 2016). The lower end of the range is generally found for freshly emitted BC, owing to the presence of non-spherical morphology. For example, Zhang et al., (2008) found that soot particles generated under incomplete combustion condition could have an effective density as low as 0.10 and 0.56 g cm^{-3} for particle size at 360 nm and 50 nm, respectively. Soot particles emitted from car brake materials, representing a typical traffic-relate source, were also found to be at a low effective density of 0.75 g cm^{-3} (Nakao et al., 2011; Nosko and Olofsson, 2017). The effective density increases immediately

https://doi.org/10.5194/acp-2021-463
Preprint. Discussion started: 22 June 2021


Atmospheric Chemistry and Physics Discussions

with aging, as a more compact morphology of BC is formed (Ghazi and Olfert, 2013; Pagels et al., 2009). For instance, a 3-10 folds increment was found for the effective density of coated soot particles compared to fresh ones, attributed to the morphology compaction verified by transmission electron microscopy (TEM) technique (Zhang et al., 2008).

Currently, there exists several techniques for the measurement of particle effective density. One commonly used method is measure particle mobility size and mass simultaneously based on differential mobility analyzer (DMA) coupled with centrifugal particle mass analyzer (CPMA) or aerosol particle mass analyzer (APM) (Geller et al., 2006; McMurry et al., 2002; Rissler et al., 2014; Wang et al., 2018), and calculate the effective density assuming a spherical morphology. Another alternative technique is based on the relationship between aerodynamic diameter and mobility diameter, measured by scanning mobility particle sizer-electrical low-pressure impactor (SMPS-ELPI) or DMA-micro-orifice uniform deposit impactor (DMA-MOUDI) (Kelly and McMurry, 1992; Nosko and Olofsson, 2017). Techniques such as connecting a mass spectrometer in series with a DMA are also applied in field studies as well as laboratory experiments, which can directly provide particle chemical composition information in addition to effective density (Spencer et al., 2007; Zhang et al., 2016a). Among the above approaches, the first one (mass-volume based method) is the most widely used in ambient measurements (Peng et al., 2021).

Measured effective densities of ambient particles with a certain diameter usually present as a broad frequency distribution. To quantify the average and diversity of the measured effective densities, a Gaussian-based unimodal fit is commonly used. However, a bimodal effective density distribution with a second density mode occurring at density below 1.00 g cm^{-3} are sometimes observed when the air is strongly affected by primary emissions (Levy et al., 2013; Ma et al., 2020). The contribution of the second density mode can reach as high as 92 % (Rissler et al., 2014). It was suggested that the second density mode is dominated by soot and can be used to infer the contribution of fresh emission as well as the morphology of freshly emitted particles (Kuwata et al., 2009). To date, only a few works performed a bimodal fit on measured effective density distribution, resulting in scarce information of the second density mode for ambient particles. In addition, most studies reported values of effective density by taking the peak of the distribution (Ma et al., 2017; Qiao et al., 2018), which hides the information of variability of the density distribution.

In this study, size-resolved effective density of ambient particles was measured with a DMA-CPMA-CPC system during Multiphase chemistry experiment in Fogs and Aerosols in the North China Plain (McFAN). A new developed flexible Gaussian fit approach is applied to separate two different density modes, and a comprehensive information of each density mode is given to fully characterize variations of effective density for ambient particles. Furthermore, measured effective density is compared with the calculated one to investigate the connections between particle effective density and chemical composition.

https://doi.org/10.5194/acp-2021-463
Preprint. Discussion started: 22 June 2021


Atmospheric Chemistry and Physics Discussions

2 Experiments

2.1 Sampling site and instrumentation

Observation of particle effective density, chemical composition and number size distribution were performed from 18 October to 1 November of 2019 at Gucheng (39°09' N, 115°44' E) inside the Ecological and Agricultural Meteorological Test Station of the Chinese Academy of Meteorological Sciences in Hebei province in China. This site is located to the southwest of Beijing (~100 km) and northeast of Baoding (~35 km). It is surrounded by agricultural fields (mainly for corn cultivation) and ~ 1 km away from the No.107 National highway. The site is influenced by both local emissions from nearby villages and regional transport, and can well represent the average pollution condition in the rural area of North China Plain (NCP) (Li et al., 2021a).

During the observation, all aerosol instruments were settled inside an air-conditioned container with a constant temperature around 24 °C. The schematic of our measurement settings is shown in Fig. S1. Ambient particles were sampled with a PM_{10} inlet and then passed through a 1.2 m long Nafion dryer and a 0.4 m long silica gel drying tube in series to reduce the relative humidity (RH) to < 30 %. A constant flowrate of 16.7 L min^{-1} in the main inlet line were maintained by a mass flow controller and an extra pump to ensure an accurate cut-off size of the inlet.

A combined DMA-CPMA-CPC system was employed to measure the size-resolved effective density of particles with mobility diameter of 50, 100, 150, 220, and 300 nm. Aerosol particles were first passed through a DMA (Model 3081, TSI Inc.) operated at a sample flowrate of 1.0 L min^{-1} and a sheath flowrate of 5.0 L min^{-1} for size classification. The output semi-monodisperse charged particles were then introduced into a CPMA (Cambustion Ltd.) followed by a CPC (Model 3772, TSI Inc.) to measure their mass distribution. It takes about one hour for a complete measurement cycle, in which frequency distributions of effective density with 22-38 bins for the 5 selected diameters were obtained. The DMA-CPMA-CPC system were calibrated using polystyrene latex (PSL) with diameter of 150, 220, and 300 nm before and after the field campaign. An uncertainty within ~ 5 % was found by comparing the measured effective density with PSL material density (1.05 g cm^{-3}) (Fig. S2).

Particle size distribution between 13-700 nm was measured by scanning mobility particle sizer (SMPS, Model 3938, TSI Inc.). The mass concentrations of non-refractory submicron aerosol (NR-PM_1) composition including OA, nitrate (NO_3^-), sulfate (SO_4^{2-}), ammonium (NH_4^+) and chloride (Cl^-) were acquired using a quadrupole aerosol chemical speciation monitor (Q-ACSM, Aerodyne Research Inc.) with a time-resolution of 30 min. The setup and calibration procedures followed that described in Ng et al., (2011). Source apportionment for organics was conducted using positive matrix factorization (PMF) algorithm, and four factors including one SOA (oxidized OA, OOA) and three POA, i.e., biomass burning OA (BBOA), cooking OA (COA) and hydrocarbon-like OA (HOA) were determined. BC mass concentration was measured with a 7-wavelength Aethalometer (Model AE33, Magee Scientific) based on the attenuation at λ = 880 nm and a corresponding mass absorption cross section of 7.77 m^2 g^{-1} (Drinovec et al., 2015).

https://doi.org/10.5194/acp-2021-463
Preprint. Discussion started: 22 June 2021


Atmospheric Chemistry and Physics Discussions

It should be noted that the effective density and size distribution data presented in our work starts from 18 October to 1 November, while chemical data are available between 18 October and 27 October. Effective density characterization in Sect. 3.1-3.3 is based on the data covering the entire observation period, and the combined analysis of density and chemical composition (Sect. 3.4) only covers the shorter period mentioned above.

2.2 Calculation of effective density

The mass-volume based method was applied in our study. Particle effective density can be calculated as:

$$\rho_{\text{eff}} = \frac{m}{\frac{\pi}{6} D_{\text{me}}^3} \quad (1)$$

where m is the particle mass measured by CPMA, D_{me} is the particle mobility size measured by DMA. It can be speculated that ρ_{eff} is equal to the material density for compact spherical particles, while ρ_{eff} is smaller than the material density for non-spherical, irregular particles or spherical but porous particles.

In contrast to previous studies mostly using unimodal Gaussian fit to process raw data of DMA-CPMA-CPC measurements, a flexible Gaussian fit algorithm with either uni- or bimodal combined with corresponding classification standard was developed in our study to better characterize the frequency distribution of particle effective density. The algorithm includes two steps.

The first step is to remove doubly charged particles. It is shown that doubly charged particles is ubiquitous and unavoidable for DMA based mobility-selected method, especially for particle size over 100 nm (Park et al., 2003). Nonetheless, doubly charged particles can be cleanly separated from singly charged particles with the same mobility size after penetrating through CPMA (McMurry et al., 2002). The theoretical masses of doubly charged particles for the five selected mobility sizes were estimated based on the Boltzmann equilibrium charge distribution (Fuchs, 1963; Wiedensohler, 1988) and listed in Table S1. For instance, doubly charged particles present a 2.8-fold higher mass value than the singly charged particles with DMA selected size of 300 nm. For each acquired particle mass distribution, the mode of doubly charged particles were discarded for the following analysis. Note that other multiply charged particles are not considered here since their mass is beyond the CPMA mass setting range.

The second step is to determine the number of modes and perform a uni- or bimodal Gaussian fit. For each effective density distribution, a bimodal Gaussian fit (Eq. 2 with $N_{\text{mode}} = 2$) was firstly implemented. If the height a_{i} of the mode located at lower density mode exceeds 5 % of that of the other mode, the fitting terminated. Otherwise, a unimodal Gaussian fit (Eq. 2 with $N_{\text{mode}} = 1$) was performed.

$$f(\rho_{\text{bin}}) = \sum_{i=1}^{N_{\text{mode}}} a_{\text{i}} \cdot \exp\left(\frac{\left(\log\rho_{\text{bin}} - \log\bar{\rho}_{\text{eff,i}}\right)^2}{2\sigma_{\text{i}}^2}\right) \quad (2)$$

where, f is the frequency distribution of effective density; ρ_{bin} is the effective density of each measured bin and is equally spaced in logarithm scale; N_{mode} is the number of modes used in the fit; $\bar{\rho}_{\text{eff,i}}$ is the geometric mean effective density of mode i; a_{i} is the height at $\bar{\rho}_{\text{eff,i}}$ of mode i; σ_{i} is the standard deviation of mode i.

https://doi.org/10.5194/acp-2021-463
Preprint. Discussion started: 22 June 2021


Atmospheric Chemistry and Physics Discussions

The bulk particle effective density ($\rho_{\mathrm{eff,ACSM}}$) was also calculated with the aerosol chemical composition measured by ACSM based on Eq. 3, assuming that ambient particles were composed of $(NH_4)_2SO_4$, NH_4NO_3, ammonium chloride (NH_4Cl), OA and BC.

$$\frac{1}{\rho_{\mathrm{eff,ACSM}}} = \sum_{i=1}^{N} \frac{f_{\mathrm{m,i}}}{\rho_{\mathrm{i}}} \quad (3)$$

where $f_{\mathrm{m,i}}$ represents the mass fraction of chemical component i; ρ_{i} is the assumed effective density of chemical component i. Densities of $(NH_4)_2SO_4$, NH_4NO_3, NH_4Cl are 1.76, 1.73 and 1.53 g cm^{-3}, respectively. The density of OA usually ranges from 1.20 to 1.60 g cm^{-3} (Dinar et al., 2006; Kostenidou et al., 2007; Turpin and Lim, 2001). In this study a fixed value of 1.30 g cm^{-3} was used in the calculation. A sensitivity test regarding the uncertainties associated with the range of OA density was conducted. Considering the large range of observed BC effective density (0.30-1.80 g cm^{-3}), a sensitivity analysis was applied to identify the optimal value of BC effective density. More discussion on OM and BC effective density can be found in Sect. 3.4.

For the comparison with $\rho_{\mathrm{eff,ACSM}}$, we also estimated the average effective density based on the measured frequency distribution of effective density as:

$$\bar{\rho}_{\mathrm{eff,tot}} = \frac{\int \rho_{\mathrm{bin}} \cdot \frac{dn}{d\log\rho_{\mathrm{bin}}} d\log\rho_{\mathrm{bin}}}{\int \frac{dn}{d\log\rho_{\mathrm{bin}}} d\log\rho_{\mathrm{bin}}} \quad (4)$$

where, $\frac{dn}{d\log\rho_{\mathrm{bin}}}$ is the measured frequency distribution of effective density.

2.3 Calculation of fractal dimension

With the identification of sub-density mode in Sect 2.2, the geometric mean of the measured mass distribution of the sub-density mode ($\bar{m}_{\mathrm{sub}}$) can be used to characterize the mass-mobility relationship in the size range of 50-300 nm. The relationship could be expressed as (Park et al., 2003)

$$\bar{m}_{\mathrm{sub}} = C d_{\mathrm{me}}^{D_{\mathrm{f}}} \quad (5)$$

where C is a constant and D_{f} is the fractal dimension, which reflects the morphology of particles. D_{f} varies from 1 to 3, increasing as particle morphology becomes less fractal and with the value of 3 for spherical particle. By fitting $\bar{m}_{\mathrm{sub}}$ and d_{me} at the five measured particle sizes, C and D_{f} can be determined. The measurement cycles containing less than 4 sizes with identified sub-density mode were excluded in the calculation to ensure the accuracy.

3 Results and discussion

3.1 Size-resolved particle effective densities

Figure 1 depicts the statistical results after averaging all effective density distributions for 50, 100, 150, 220 and 300 nm particle sizes. Based on the flexible Gaussian fit, a considerable amount (77 %-87 %) of bimodal distribution condition

https://doi.org/10.5194/acp-2021-463
Preprint. Discussion started: 22 June 2021


Atmospheric Chemistry and Physics Discussions

occurred for all size particles. The first peak is found to be located below 0.90 g cm^{-3}, and the second is higher than 1.20 g cm^{-3}. For a compositional mixed compact spherical particle, particle density speculated from the material density of each individual component is supposed to be higher than 1.20 g cm^{-3} (the lowest material density among all components is 1.20 g cm^{-3}, Ma et al., 2017; Xie et al., 2017). However, a low-density mode with peak density less than 1.00 g cm^{-3} usually exists for freshly emitted particles, indicating the presence of particles with highly agglomerated or porous morphology (Park et al., 2003; Rissler et al., 2013). Therefore, the two density modes observed in this study are defined as: (1) "sub-density" referred to low effective density mode, implying particles' feature of fractal aggregated; (2) "main-density" referred to relatively high effective density mode with a dense or compact particle structure.

As listed in Table 1, the occurrence frequencies of the sub-density mode are 79 %, 87 %, 86 %, 77 %, and 81 % for particle diameters of 50, 100, 150, 220, and 300 nm, respectively. These frequencies are significantly higher than those reported in Levy et al., (2013) which only reach up to 32 % for 150 nm particles in an inner-city in Houston. It is also different from another study conducted in suburban environment of Nanjing, China (Ma et al., 2017), where they observed a dominant unimodal distribution of effective density with only < 10 % occurrence with bimodal distribution. On the other hand, a low effective density mode (density < 1.20 g cm^{-3}) exists or even dominates in the measurements near emission sources (Nosko and Olofsson, 2017; Olfert and Rogak, 2019; Park et al., 2003), which is ascribed to freshly emitted or partial aged BC and non-uniformly mixed particles. The remarkably high occurrence of the sub-density mode in our study indicates a frequent influence of local BC emission. Meanwhile, the discrepancy in observed frequencies of the sub-density mode with other studies can be explained, to some extent, by different thresholds used in the studies to identify bimodal distribution of effective density. In our study, we aim at identifying as more bimodal cases as possible with a low threshold of 5 % as mentioned in Sect. 2.2.

On the basis of bimodal Gaussian fit, the number fraction of the sub-density mode particles (F_{sub}) can be determined. The mean (min., max.) values of F_{sub} are 27 % (4 %, 88 %), 22 % (5 %, 63 %), 23 % (6 %, 64 %), 23 % (9 %, 85 %), 25 % (5 %, 78 %) for 50, 100, 150, 220 and 300 nm particle size, respectively (Table 1), showing no obvious trend with particle size. The results in our study are lower than those (11 %-92 %, with most cases exceeding 50 %) in traffic emission influenced sites (Geller et al., 2006; Rissler et al., 2014), as the number fraction of the sub-density mode is tightly related to the influence of fresh BC emission sources (Geller et al., 2006; Levy et al., 2014; Ma et al., 2020).

During the entire campaign, the geometric mean for the main-density mode ($\bar{\rho}_{\mathrm{eff,main}}$) vary from 0.94 to 1.42, 1.01 to 1.47, 1.09 to 1.48, 1.16 to 1.59, 1.22 to 1.73 g cm^{-3} for particles at 50, 100, 150, 220 and 300 nm respectively, and for the sub-density mode ($\bar{\rho}_{\mathrm{eff,sub}}$) vary from 0.74 to 1.20, 0.59 to 1.25, 0.55 to 1.14, 0.36 to 0.99, 0.34 to 1.00 g cm^{-3}, respectively. Although the temporal variations are similar for the five measured sizes, densities of particles at 50 and 100 nm show greater variability than larger ones (Fig. S3).

$\bar{\rho}_{\mathrm{eff,main}}$ exhibits an evident ascending trend with particle size (Fig. 2), similar to the pattern reported in Shanghai (Yin et al., 2015). This is probably affected by two aspects. One is the increase of the proportion of high-density components with

https://doi.org/10.5194/acp-2021-463
Preprint. Discussion started: 22 June 2021


Atmospheric Chemistry and Physics Discussions

increasing particle size, from OA dominant to secondary inorganic aerosol (SIA) dominant. Although size-resolved chemical composition was not measured in this study, it can be inferred from Li et al., (2021b) that the mass fraction of SIA increased from 49 % (49 %) to 55 % (61 %) with particle size increasing from 150 to 300 nm in autumn (winter) in the NCP. The other is the collapse and restructuring effect occurred for soot-containing particles during aging processes (Ghazi and Olfert, 2013; Pagels et al., 2009), leading to a more spherical-like or more dense morphology of large particles.

However, $\bar{\rho}_{\mathrm{eff,sub}}$ decreases from 0.89 g cm^{-3} to 0.62 g cm^{-3} as particle size increases from 50 to 300 nm. This can be ascribed to the agglomerate effect that fresh soot particles with larger sizes are more agglomerated and hence have a larger fractal dimension and lower effective density. This has been confirmed by TEM images for diesel engine exhaust particles (Park et al., 2003) and traffic-related environmental samples (Rissler et al., 2014). Figure 2 also shows the results for fresh soot from previous studies. All the reported densities of freshly emitted particles from diesel combustion, aircraft, and other burning sources show decreasing trends with particle size, but with much steeper slopes than our results. This is because after emitted into the atmosphere, fresh soot is rapidly coated with $(NH_4)_2SO_4$, NH_4NO_3 and OA (Kuwata et al., 2009), leading to an increasing $\bar{\rho}_{\mathrm{eff,sub}}$ and less pronounced decline trend compared with observations for primary sources (Olfert et al., 2007; Tavakoli and Olfert, 2014; Ubogu et al., 2018).

Most previous studies did not differentiate the two modes and reported either an overall increasing (Levy et al., 2014; Ma et al., 2020; Yin et al., 2015) or decreasing trends (Geller et al., 2006; Qiao et al., 2018) of $\bar{\rho}_{\mathrm{eff}}$ with particle size. A unimodal distribution implies an assumption of an internal mixing of particles, which is not true since most surface atmosphere is affected by fresh emissions. Therefore, the feature of the sub-density mode may be missed if a unimodal fit is used. As shown in Fig. 2, only a slightly monotonically increasing trend of the average effective density ($\bar{\rho}_{\mathrm{eff,tot}}$) with particle size are observed (grey dotted line in Fig. 2). Therefore, sub-density modes need to be isolated to reflect the detailed features of effective density of ambient particles. Furthermore, bimodal fits can also provide additional information on the mixing state of fresh and aged particles.

In addition to the size dependence of $\bar{\rho}_{\mathrm{eff,main}}$ and $\bar{\rho}_{\mathrm{eff,sub}}$, σ of different effective density modes also varies with particle size. The mean σ of the main-density mode are similar for particles in the size range of 50 to 150 nm (~0.053), and gradually increases to 0.067 at 300 nm (Table 1). The mean σ of the sub-density mode demonstrates the highest value (~0.215) at 300 nm, and decreases to ~0.044 at 50 nm. Since particles usually appear as more dense morphology in the main-density mode (Rissler et al., 2014), the variation of σ probably originates from the differences in particle chemical composition. For the sub-density mode, soot is the main component of particles (approximately over 80 %, Kuwata et al., 2009). It has been found that the morphology of freshly emitted soot is more chain-like at large particle sizes than at small sizes (e.g., Park et al., 2003). We therefore speculate that the chain-like morphology enables a higher degree of morphological variation of larger particles, resulting in a broader sub-density distribution.

https://doi.org/10.5194/acp-2021-463
Preprint. Discussion started: 22 June 2021


Atmospheric Chemistry and Physics Discussions

3.2 Effective density at polluted and clean conditions

Given that the particle effective density varies dramatically with time (Fig. S3), the entire sampling period is classified into two groups according to the volume concentration of $PM_{0.7}$: (i) a polluted group with volume concentration higher than 50 $\mu m^3\ cm^{-3}$, and (ii) a clean group corresponding to volume concentration lower than 50 $\mu m^3\ cm^{-3}$. The average effective density distributions of the two groups are depicted in Fig. 3 and the statistics of the $\bar{\rho}_{\mathrm{eff,main}}$ and $\bar{\rho}_{\mathrm{eff,sub}}$, as well as F_{sub} and occurrence frequency of the sub-density mode are given in Table 2. $\bar{\rho}_{\mathrm{eff,main}}$ in the polluted group for each particle size is 0.08-0.11 g cm^{-3} lower than that in the clean group. In contrast, the difference of $\bar{\rho}_{\mathrm{eff,sub}}$ is insignificant with the maximum discrepancy of 0.03 g cm^{-3}, which is only one-third of the maximum discrepancy for $\bar{\rho}_{\mathrm{eff,main}}$. The size dependence of $\bar{\rho}_{\mathrm{eff,main}}$ and $\bar{\rho}_{\mathrm{eff,sub}}$ follows the similar pattern under all conditions (Fig. S4).

It can be noted from Table 2 that F_{sub} varies with pollution levels. In the clean group, F_{sub} mainly distributes over a small range of 21 %-26 %, with little size dependence; while in the polluted group, F_{sub} gradually decreases from 42 % at 50 nm to 18 % at 300 nm. This is consistent with the observations conducted by Rissler et al. (2014) in Copenhagen, which showed a decrease around 50 % in the number fraction of fresh soot particles (equivalent to F_{sub} in our study) from 75 nm to 350 nm under heavily polluted condition. Since the integrated area of the sub-density mode at each particle size are stable in the polluted group, the size dependence of F_{sub} is mainly driven by the increase in the integrated area of the main-density mode with particle size. As a result, F_{sub} for particles at 50-100 nm is higher in the polluted group than clean group, but it is opposite for particles at 150-300 nm.

Similarly, the occurrence frequency of the sub-density mode decreases with particle size (with an exception of 50 nm) in the polluted group: 72 %, 95 %, 89 %, 63 %, and 57 % at 50, 100, 150, 220 and 300 nm, respectively. In contrast, the variation with particle size in the clean group is no more than 10 %. One possible explanation is that the sub-density mode inherently diminishes due to higher aging degree for larger particles under polluted condition. Xie et al., (2017) found that the effective density distribution was more inclined to a unimodal distribution for particles at 220 nm than 40 nm during episodes at PM_1 volume concentrations above 50 $\mu m^3\ cm^{-3}$. Hence, the occurrence probability of bimodal distribution was expected to be higher for smaller particles with respect to large particles, similar to the results in this study. Additionally, it is difficult to identify the sub-density mode as it falls below the threshold defined in Sect. 2.2 due to the increasing contribution of the main-density mode for larger particles, which consequently reduces the corresponding occurrence frequency of the sub-density mode.

3.3 Diurnal variations of effective density

Figure 4 describes the diurnal cycle of $\bar{\rho}_{\mathrm{eff,main}}$ and $\bar{\rho}_{\mathrm{eff,sub}}$ at the five measured particles sizes. $\bar{\rho}_{\mathrm{eff,main}}$ increases in the morning and gradually decreases in the late afternoon and early evening for all particle sizes. The upward tendency in the morning and early afternoon is associated with the increasing intensity of secondary aerosol production, resulting in an

https://doi.org/10.5194/acp-2021-463
Preprint. Discussion started: 22 June 2021


Atmospheric Chemistry and Physics Discussions

increment of high material density components, such as SIA and OOA mass fraction, especially of NH_4NO_3 (Fig. S5). Besides, with the increase in the fraction of internally mixed particles and coating thickness (Cheng et al., 2012; Ma et al., 2012), particles gradually approach spherical-like morphology (Ghazi and Olfert, 2013; Pagels et al., 2009), which also leads to the increase of $\bar{\rho}_{\mathrm{eff,main}}$. In the late afternoon, $\bar{\rho}_{\mathrm{eff,main}}$ starts to decline, attributed to elevated mass fractions of BC and POA (Fig. S5) due to enhanced emissions from traffic, biomass burning, and cooking identified by PMF.

The diurnal cycle of $\bar{\rho}_{\mathrm{eff,sub}}$ is similar to that of $\bar{\rho}_{\mathrm{eff,main}}$ for each particle size, with a daily maximum observed in the early afternoon and a relatively low level in the night. One difference between the two modes is that $\bar{\rho}_{\mathrm{eff,sub}}$ drops more rapidly before sunset compared with $\bar{\rho}_{\mathrm{eff,main}}$, especially for large particles ($\geq$ 150 nm). This is because the sub-density mode is more directly related with freshly emitted particles than the main-density mode.

The diurnal cycle of F_{sub} is different from the pattern of $\bar{\rho}_{\mathrm{eff,main}}$ and $\bar{\rho}_{\mathrm{eff,sub}}$. As shown in Fig. 4f, F_{sub} exhibits insignificant daily variability for particles at 50-100 nm, while double peaks are observed in the morning and evening for particles at 150-300 nm associated with large amount of fresh BC emissions. The minimum F_{sub} for particles at 150-300 nm is generally found during the mid-afternoon, e.g. 15 % at 14:00 for 300 nm. This is consistent with the pattern of the occurrence frequency of the sub-density mode, which drops remarkably during 12:00-16:00 (Fig. S6). The drop of both F_{sub} and occurrence frequency could be explained by the transition of particles from the sub-density mode to the main-density mode associated with aging processes.

As shown in Fig. 5, D_{f} shows a distinct diurnal variation. There are two decreasing trends: from 06:00 to 11:00, and from 17:00 to 19:00, corresponding to the morning and evening rushing hours, with D_{f} falling into the range of particles from vehicle emissions (2.22-2.84) reported in previous studies (Wu et al., 2019, Olfert et al., 2007; Park et al., 2003). The rapid increase in D_{f} from 2.62 (11:00) to 2.86 (13:00) at noon could be attributed to photochemical aging, resulting in more compact particles (Ghazi and Olfert, 2013). During early afternoon (14:00-16:00), there is no D_{f} values due to a sharp reduction in occurrence frequency of the sub-density mode (Fig. S6) as discussed above. D_{f} gradually increases from 2.51 at 19:00 to 2.81 at 24:00, probably associated with aging processes during the night. It is worth noting that the increase rate of D_{f} differs between noon and night, being ~0.12 h^{-1} at noon, which is twice of the night-time rate (0.06 h^{-1}). It indicates that photochemical aging process is very efficient in transiting particles from fractal to compact morphology. In addition, D_{f} stays at around 2.8 during 00:00-05:00.

3.4 Influence of chemical composition on effective density

Chemical composition is one of the key factors affecting particle density. Inorganic components including NH_4NO_3 and $(NH_4)_2SO_4$ have higher density than OA and BC. Therefore, the variation in aerosol chemical composition can, to some extent, explain the wide range of observed effective density. Since 300 nm is the closest one to the peak position of particle volume distribution (Fig. S7) among all the five measured sizes, the average effective density of particles at 300 nm

https://doi.org/10.5194/acp-2021-463
Preprint. Discussion started: 22 June 2021


Atmospheric Chemistry and Physics Discussions

($\bar{\rho}_{\mathrm{eff,tot,300nm}}$) is used to compare with the ACSM-derived bulk effective density ($\rho_{\mathrm{eff,ACSM}}$) based on Eq. 3 to understand the connection between particle effective density and chemical composition.

As mentioned earlier, there exists large variation in BC effective density due to the influence of morphology, but most studies have ignored the influence of BC effective density or just used a material density of 1.80 g cm^{-3} for BC (Lee et al., 2013; Levy et al., 2013; Lin et al., 2018). And assuming a dense spherical BC with density of 1.80 g cm^{-3} may even lead to ~17 % overestimation of absorption enhancement (Zhang et al., 2016b). To analysis the influence of BC effective density on $\rho_{\mathrm{eff,ACSM}}$, a sensitivity test with BC effective density ranging from 0.30 to 1.80 g cm^{-3} and a step size of 0.05 g cm^{-3} is performed in this study. The minimum value (0.30 g cm^{-3}) is the lowest effective density of BC at 300 nm observed in the atmosphere (Olfert et al., 2017) while the maximum (1.80 g cm^{-3}) is the material density of BC. The mean square error (MSE) and R-square (R^2) between $\bar{\rho}_{\mathrm{eff,tot,300nm}}$ and $\rho_{\mathrm{eff,ACSM}}$ at each BC density step are shown in Fig. 6a. In addition, Fig. 6b shows the comparison between $\bar{\rho}_{\mathrm{eff,tot,300nm}}$ and $\rho_{\mathrm{eff,ACSM}}$ with assumed BC effective density of 0.30, 0.60, 1.00 and 1.80 g cm^{-3}, respectively.

We find that $\rho_{\mathrm{eff,ACSM}}$ can be decreased on average by 40 % if the applied BC effective density changes from 1.80 to 0.30 g cm^{-3}. In addition, there is 34 % of observed $\bar{\rho}_{\mathrm{eff,tot,300nm}}$ with values below 1.20 g cm^{-3}, which could only be explained by low BC effective density. Therefore, applying a proper BC effective density is crucial for accurate estimates of the effective density of ambient particles. Among all tested values, $\rho_{\mathrm{eff,ACSM}}$ with assumed BC effective density of 0.60 g cm^{-3} matches best with measured $\bar{\rho}_{\mathrm{eff,tot,300nm}}$ (R^2 = 0.62 and MSE = 0.014). Well correlation with R^2 of 0.62 (0.61) is found for BC effective density of 0.30 g cm^{-3} (or 1.00 g cm^{-3}), but the MSE reaches up to 0.088 (0.048). In contrast, when using a BC effective density of 1.80 g cm^{-3}, the derived $\rho_{\mathrm{eff,ACSM}}$ is much higher than the measured $\bar{\rho}_{\mathrm{eff,tot,300nm}}$ and there is barely any correlation between them. Therefore, a fixed BC effective density of 0.60 g cm^{-3}, which is only one third of its material density, is preferred for the $\rho_{\mathrm{eff,ACSM}}$ calculation in the following analysis.

Additionally, a sensitivity test for OA density ranging from 1.20 to 1.60 g cm^{-3} (Dinar et al., 2006; Kostenidou et al., 2007; Turpin and Lim, 2001) is conducted as well to evaluate the uncertainties associated with the variability of OA density. As seen in Fig. S8, the changes in OA density have little influence on $\rho_{\mathrm{eff,ACSM}}$ (difference within 8 %) for the test OA density range. The MSE associated with OA densities is an order of magnitude lower than that with BC densities, and reaches minimum for OA density of ~1.20-1.30 g cm^{-3}. The R^2 at each OA density maintains around 0.62. The results suggest insignificant influence associated with the variation of OA density, in contrast to BC, and the selection of OA density of 1.30 g cm^{-3} is appropriate for the effective density calculation of ambient particles.

As shown in Fig. 6b, while the majority of data points are clustered near the 1:1 line, there exists some anomalous points deviated from the 1:1 line. Appling a PM_1 threshold of 60 μg m^{-3}, the data sets can be classified into two groups: (i) a consistent pair with a slope of 1.16 and R^2 of 0.65 for relatively clean condition ($PM_1 \leq 60$ μg m^{-3}), and (ii) uncorrelated set with R^2 of 0.10 for polluted condition ($PM_1 > 60$ μg m^{-3}) (Fig. 7). This implies that $\bar{\rho}_{\mathrm{eff,tot,300nm}}$ could be used as a proxy for

https://doi.org/10.5194/acp-2021-463
Preprint. Discussion started: 22 June 2021


Atmospheric Chemistry and Physics Discussions

bulk effective density under clean condition but not polluted condition. A correlation analysis is then conducted to further evaluate the influence of chemical composition on the $\bar{\rho}_{\mathrm{eff,tot,300nm}}$ under clean condition. As shown in Fig. 8a, there is an obvious positive correlation (R^2 = 0.52 and slope = 0.01) between $\bar{\rho}_{\mathrm{eff,tot,300nm}}$ and SIA mass fraction, indicating that particle densities are largely dependent on SIA, consistent with Yin's and Zhang's study (Yin et al., 2015; Zhang et al., 2016a). On the contrary, a notable negative correlation is observed between $\bar{\rho}_{\mathrm{eff,tot,300nm}}$ and BC mass fraction with R^2 of 0.65 and slope of -0.02 (Fig. 8b). The magnitude of both the correlation coefficient and the slope for BC is higher than SIA, implying a stronger influence of BC on the effective density compared with SIA. This further confirms the importance and necessity of including BC in the estimate of effective density for ambient particles. In addition, the correlation is poor between $\bar{\rho}_{\mathrm{eff,tot,300nm}}$ and other chemical components.

To better indicate the variation of effective density with particle chemical composition, a sensitivity test is conducted based on arbitrarily assumed mass fractions for each component. Considering the major contribution of NH_4NO_3 in SIA, only one density of 1.73 g cm^{-3} is used for total SIA, and the test is thus performed with a 3-component (SIA, BC and OA) parameterization. The results are presented in Fig. 9, with the fractions of BC and SIA labelled on the x and y-axis, respectively, whereas the fractions of OA could be deduced as the rest. Calculated ρ_{eff} spreads from 0.60 to 1.73 g cm^{-3}, corresponding to 100 % of BC and SIA, respectively, similar to the measured range of 0.64-1.64 g cm^{-3} for $\bar{\rho}_{\mathrm{eff,tot,300nm}}$. In general, ρ_{eff} increases as the BC fraction decreases or SIA fraction increases. It is interesting to note that ρ_{eff} is more sensitive to BC as the fraction of BC decreases. In addition, when BC fraction < 30 %, which is generally observed in the ambient (Ding et al., 2016; Yang et al., 2011), ρ_{eff} is much more sensitive to the changes in BC fractions rather than SIA fractions, consistent with the results based on the correlation analysis under clean condition.

In the case of polluted condition, $\bar{\rho}_{\mathrm{eff,tot,300nm}}$ is concentrated close to 1.20 g cm^{-3} with a standard deviation of 0.04, while $\rho_{\mathrm{eff,ACSM}}$ varies in the range of 1.17-1.47 g cm^{-3} (~0 %-22 % higher than $\bar{\rho}_{\mathrm{eff,tot,300nm}}$). The difference can be attributed to the discrepancies of chemical composition between bulk PM_1 and particles with size of 300 nm. Compared with clean condition, an increase of 12.5 % in SIA mass fraction (dominated by NH_4NO_3) and a decrease of 6.1 % in BC mass fraction in bulk PM_1 is observed during the polluted periods (Fig. S9). The mass concentration of SIA increased from 20 to 64 μg m^{-3} and most of the additional mass might be added to particles with size larger than 300 nm (Yan et al., 2021). This could be indicated by the change in particle volume size distribution (Fig. S7), which shows a decrease of volume fraction for particles with size < 300 nm in $PM_{0.7}$ from 43 % at clean condition to 29 % at polluted condition. This shift towards larger particles under polluted condition makes the difference in chemical composition between PM_1 and particles at size of 300 nm noticeable and thus results in the inconsistence between $\bar{\rho}_{\mathrm{eff,tot,300nm}}$ and $\rho_{\mathrm{eff,ACSM}}$.

Since NH_4NO_3 and BC exhibit the largest difference between polluted and clean conditions (Fig. S9), a sensitivity study with scale factors ranging from 0.01 to 5 applied for the two components is performed for polluted condition to help explain the discrepancy between $\bar{\rho}_{\mathrm{eff,tot,300nm}}$ and $\rho_{\mathrm{eff,ACSM}}$ (Fig. 7a). Figure 10 shows the ratios of new calculated $\rho_{\mathrm{eff,ACSM}}$ versus

https://doi.org/10.5194/acp-2021-463
Preprint. Discussion started: 22 June 2021


Atmospheric Chemistry and Physics Discussions

$\bar{\rho}_{\mathrm{eff,tot,300nm}}$ as well as the new fractions of NH_4NO_3 and BC in bulk PM_1 obtained with different scale factors. The original mean fractions of NH_4NO_3 and BC in bulk PM_1 under polluted condition are 56.9 % and 10.3 %, respectively (shown as red circles in Fig. 10). Assuming the increase in NH_4NO_3 occurs mainly in particles with size larger than 300 nm, the "true" fraction of NH_4NO_3 in particles with size of 300 nm would decrease while the one of BC would increase (a shift toward top-left of the plots from the original position in Fig. 10). Consequently, the discrepancy between $\rho_{\mathrm{eff,ACSM}}$ and $\bar{\rho}_{\mathrm{eff,tot,300nm}}$ would be reduced, with the ratios of new derived $\rho_{\mathrm{eff,ACSM}}$ versus $\bar{\rho}_{\mathrm{eff,tot,300nm}}$ close to 1.

4 Conclusion

Effective density, as one of important physical properties of aerosol particles, is highly related with particle morphology and chemical composition. Here we report size-resolved particle effective density observed during McFAN in autumn of 2019 in the rural area of the North China Plain. Combined with number size distribution and chemical composition measured in parallel, the study fully characterizes size-resolved particle effective density and its evolution associated with emissions and aging processes.

With a new developed flexible Gaussian fit algorithm, the study identified frequent bimodal distribution of particle effective density, accounting for 77 %-87 % of total observations. The two modes are then defined as a sub-density mode and a main density mode. The number fraction of sub-density mode particles (F_{sub}) is 22 %-27 % for the five measured sizes, indicating the importance of distinguishing the main- and sub-density mode. The prevalence of the sub-density mode is closely related to fresh black carbon (BC) emissions.

During the whole campaign, opposite size-dependency trend is found for the geometric mean of the main- and sub-density mode ($\bar{\rho}_{\mathrm{eff,main}}$ and $\bar{\rho}_{\mathrm{eff,sub}}$, respectively). $\bar{\rho}_{\mathrm{eff,main}}$ increases from 1.18 g cm^{-3} (50 nm) to 1.37 g cm^{-3} (300 nm) due to larger fraction of high-density components and more significant restructuring effect at large particle sizes, while $\bar{\rho}_{\mathrm{eff,sub}}$ decreases from 0.89 g cm^{-3} (50 nm) to 0.62 g cm^{-3} (300 nm) ascribed to the agglomerate effect. The mean σ of the sub-density mode is higher than that of the main-density mode (except for 50 nm), and the mean σ of both modes increases with particle size in general.

$\bar{\rho}_{\mathrm{eff,main}}$ in the polluted group for each particle size is 0.08-0.11 g cm^{-3} lower than that in the clean group. In contrast, the difference of $\bar{\rho}_{\mathrm{eff,sub}}$ is insignificant with the maximum of 0.03 g cm^{-3}. In addition, both F_{sub} and the occurrence frequency of the sub-density mode generally decrease with particle size in polluted condition, while both parameters present little size dependence in clean condition.

There also exits obvious diurnal cycle for both $\bar{\rho}_{\mathrm{eff,main}}$ and $\bar{\rho}_{\mathrm{eff,sub}}$, with maximum in the early afternoon and a relatively low level in the night. The peaks could be attributed to the increasing mass fraction of high material density components (e.g. OOA and SIA) associated with secondary aerosol production. We find that both of F_{sub} and occurrence frequency of the sub-

https://doi.org/10.5194/acp-2021-463
Preprint. Discussion started: 22 June 2021


Atmospheric Chemistry and Physics Discussions

density mode drops remarkably in the afternoon, suggesting the transition of particles from the sub-density mode to the main-density mode associated with aging processes.

To investigate the impact of chemical composition, we compare the average effective density of particles at 300 nm ($\bar{\rho}_{\mathrm{eff,tot,300nm}}$) with the ACSM-derived bulk effective density ($\rho_{\mathrm{eff,ACSM}}$). The best agreement between $\bar{\rho}_{\mathrm{eff,tot,300nm}}$ and $\rho_{\mathrm{eff,ACSM}}$ is achieved with assumed BC effective density of 0.6 g cm^{-3}. On the other hand, the comparison is found to be insensitive to the changes in assumed OA effective density.

The comparison between $\rho_{\mathrm{eff,ACSM}}$ and $\bar{\rho}_{\mathrm{eff,tot,300nm}}$ is different for polluted and clean conditions. Under clean conditions, $\bar{\rho}_{\mathrm{eff,tot,300nm}}$ is well correlated with $\rho_{\mathrm{eff,ACSM}}$ with a slope close to 1, indicating that $\bar{\rho}_{\mathrm{eff,tot,300nm}}$ could be used as a proxy for bulk effective density under clean condition. In contrast, $\bar{\rho}_{\mathrm{eff,tot,300nm}}$ concentrated at 1.20 g cm^{-3} but $\rho_{\mathrm{eff,ACSM}}$ varies from 1.17 to 1.47 g cm^{-3} under polluted conditions. This poor comparison is likely to stem from relatively larger discrepancy of chemical composition in bulk particle and 300 nm particles. Based on the analysis of the correlation between $\bar{\rho}_{\mathrm{eff,tot,300nm}}$ and individual chemical components, SIA and BC mass fractions are found to be the major factors determining particle densities. Moreover, the influence of BC on the effective density is even stronger than SIA, implying the importance and necessity of including BC in the estimate of effective density for ambient particles.

Data availability

The data used in this study are available from the corresponding author upon reasonable request.

Author contribution

NM and QW conceived this research. YC, HS, QZ, PF, NM, and QW planned the McFAN campaign. YZ, CC, JT, JH, LX and SZ conducted the field measurement. YZ performed the data analysis. The written article was prepared by YZ, NM, QW and ZW with input from all other co-authors.

Competing interests

The authors declare that they have no conflict of interest.

Acknowledgements

This work was supported by the National Natural Science Foundation of China (41877303 and 41907182), the Foundation of State Key Laboratory of Loess and Quaternary Geology, Institute of Earth Environment, CAS (SKLLOG2029), the Guangdong Innovative and Entrepreneurial Research Team Program (Research team on atmospheric environmental roles

and effects of carbonaceous species: 2016ZT06N263), and the Guangdong-Hongkong-Macau Joint Laboratory of Collaborative Innovation for Environmental Quality.

References

Abegglen, M., Durdina, L., Brem, B., Wang, J., Rindlisbacher, T., Corbin, J., Lohmann, U., and Sierau, B.: Effective density and mass–mobility exponents of particulate matter in aircraft turbine exhaust: Dependence on engine thrust and particle size, J. Aerosol. Sci., 88, 135-147, https://doi.org/10.1016/j.jaerosci.2015.06.003, 2015.

Bahreini, R., Keywood, M. D., Ng, N. L., Varutbangkul, V., Gao, S., Flagan, R. C., Seinfeld, J. H., Worsnop, D., and Jimenez, J.: Measurements of secondary organic aerosol from oxidation of cycloalkenes, terpenes, and m-xylene using an Aerodyne aerosol mass spectrometer, Environ. Sci. Technol., 39, 5674-5688, https://doi.org/10.1021/es048061a, 2005.

Cha, Y. and Olofsson, U.: Effective density of airborne particles in a railway tunnel from field measurements of mobility and aerodynamic size distributions, Aerosol. Sci. Tech., 52, 886-899, https://doi.org/10.1080/02786826.2018.1476750, 2018.

Cheng, Y., Su, H., Rose, D., Gunthe, S., Berghof, M., Wehner, B., Achtert, P., Nowak, A., Takegawa, N., Kondo, Y., Shiraiwa, M., Gong, Y., Shao, M., Hu, M., Zhu, T., Zhang, Y., Carmichael, G., Wiedensohler, A., Andreae, M., and Poeschl, U.: Size-resolved measurement of the mixing state of soot in the megacity Beijing, China: diurnal cycle, aging and parameterization, Atmos. Chem. Phys., 12, 4477-4491, https://doi.org/10.5194/acp-12-4477-2012, 2012.

Dinar, E., Mentel, T., and Rudich, Y.: The density of humic acids and humic like substances (HULIS) from fresh and aged wood burning and pollution aerosol particles, Atmos. Chem. Phys., 6, 5213-5224, https://doi.org/10.5194/acp-6-5213-2006, 2006.

Ding, A., Huang, X., Nie, W., Sun, J., Kerminen, V. M., Petäjä, T., Su, H., Cheng, Y., Yang, X. Q., Wang, M., Chi, X., Wang, J., Virkkula, A., Guo, W., Yuan, J., Wang, S., Zhang, R., Wu, Y., Song, Y., Zhu, T., Zilitinkevich, S., Kulmala, M., and Fu, C.: Enhanced haze pollution by black carbon in megacities in China, Geophys. Res. Lett., 43, 2873-2879, https://doi.org/10.1002/2016GL067745, 2016.

Ditas, J., Ma, N., Zhang, Y., Assmann, D., Neumaier, M., Riede, H., Karu, E., Williams, J., Scharffe, D., Wang, Q., Saturno, J., Schwarz, J. P., Katich, J. M., McMeeking, G. R., Zahn, A., Hermann, M., Brenninkmeijer, C. A. M., Andreae, M. O., Poschl, U., Su, H., and Cheng, Y.: Strong impact of wildfires on the abundance and aging of black carbon in the lowermost stratosphere, P. Natl. Acad. Sci. USA., 115, E11595-E11603, https://doi.org/10.1073/pnas.1806868115, 2018.

Dockery, D. W. and Pope, C. A.: Acute respiratory effects of particulate air pollution, Annu. Rev. Publ. Health., 15, 107-132, https://doi.org/10.1146/annurev.pu.15.050194.000543, 1994.

Drinovec, L., Močnik, G., Zotter, P., Prévôt, A., Ruckstuhl, C., Coz, E., Rupakheti, M., Sciare, J., Müller, T., Wiedensohler, A., and Hansen, A.: The" dual-spot" Aethalometer: an improved measurement of aerosol black carbon with real-time loading compensation, Atmos. Meas. Tech., 8, 1965-1979, https://doi.org/10.5194/amt-8-1965-2015, 2015.

Fuchs, N.: On the stationary charge distribution on aerosol particles in a bipolar ionic atmosphere, Pure. Appl. Geophys., 56, 185-193, https://doi.org/10.1007/BF01993343, 1963.

Geller, M., Biswas, S., and Sioutas, C.: Determination of particle effective density in urban environments with a differential mobility analyzer and aerosol particle mass analyzer, Aerosol. Sci. Tech., 40, 709-723, https://doi.org/10.1080/02786820600803925, 2006.

George, I. and Abbatt, J.: Chemical evolution of secondary organic aerosol from OH-initiated heterogeneous oxidation, Atmos. Chem. Phys., 10, 5551-5563, https://doi.org/10.5194/acp-10-5551-2010, 2010.

Ghazi, R. and Olfert, J.: Coating mass dependence of soot aggregate restructuring due to coatings of oleic acid and dioctyl sebacate, Aerosol. Sci. Tech., 47, 192-200, https://doi.org/10.1080/02786826.2012.741273, 2013.

Hallquist, M., Wenger, J. C., Baltensperger, U., Rudich, Y., Simpson, D., Claeys, M., Dommen, J., Donahue, N., George, C., Goldstein, A., Hamilton, J., Herrmann, H., Hoffmann, T., Iinuma, Y., Jang, M., Jenkin, M., Jimenez, J., Kiendler-Scharr, A., Maenhaut, W., McFiggans, G., Mentel, T. F., Monod, A., Prevot, A., Seinfeld, J., Surratt, J., Szmigielski, R., and Wildt, J.: The formation, properties and impact of secondary organic aerosol: current and emerging issues, Atmos. Chem. Phys., 9, 5155-5236, https://doi.org/10.5194/acp-9-5155-2009, 2009.

Hu, M., Peng, J., Sun, K., Yue, D., Guo, S., Wiedensohler, A., and Wu, Z.: Estimation of size-resolved ambient particle density based on the measurement of aerosol number, mass, and chemical size distributions in the winter in Beijing, Environ. Sci. Technol., 46, 9941-9947, https://doi.org/10.1021/es204073t, 2012.

IPCC: Climate Change 2007: Synthesis Report. Contribution of Working Groups I, II and III to the Fourth Assessment Report of the Intergovernmental Panel on Climate Change, Core Writing Team, edited by: Pachauri, R. K. and Reisinger, A., IPCC, Geneva, Switzerland, 104 pp., 2007.

Kelly, W. and McMurry, P. H.: Measurement of particle density by inertial classification of differential mobility analyzer–generated monodisperse aerosols, Aerosol. Sci. Tech., 17, 199-212, https://doi.org/10.1080/02786829208959571, 1992.

Kostenidou, E., Pathak, R. K., and Pandis, S. N.: An algorithm for the calculation of secondary organic aerosol density combining AMS and SMPS data, Aerosol. Sci. Tech., 41, 1002-1010, https://doi.org/10.1080/02786820701666270, 2007.

Kuwata, M., Kondo, Y., and Takegawa, N.: Critical condensed mass for activation of black carbon as cloud condensation nuclei in Tokyo, J. Geophys. Res. Atmos., 114, D20202, https://doi.org/10.1029/2009JD012086, 2009.

Laden, F., Neas, L. M., Dockery, D. W., and Schwartz, J.: Association of fine particulate matter from different sources with daily mortality in six US cities, Environ. Health. Persp., 108, 941-947, https://doi.org/10.1289/ehp.00108941, 2000.

Lee, B. P., Li, Y. J., Flagan, R. C., Lo, C., and Chan, C. K.: Sizing characterization of the fast-mobility particle sizer (FMPS) against SMPS and HR-ToF-AMS, Aerosol. Sci. Tech., 47, 1030-1037, https://doi.org/10.1080/02786826.2013.810809, 2013.

Levy, M. E., Zhang, R., Khalizov, A. F., Zheng, J., Collins, D. R., Glen, C. R., Wang, Y., Yu, X. Y., Luke, W., Jayne, J. T., and Olaguer, E.: Measurements of submicron aerosols in Houston, Texas during the 2009 SHARP field campaign, J. Geophys. Res. Atmos., 118, 10,518-510,534, https://doi.org/10.1002/jgrd.50785, 2013.

Levy, M. E., Zhang, R., Zheng, J., Tan, H., Wang, Y., Molina, L. T., Takahama, S., Russell, L., and Li, G.: Measurements of submicron aerosols at the California–Mexico border during the Cal–Mex 2010 field campaign, Atmos. Environ., 88, 308-319, https://doi.org/10.1016/j.atmosenv.2013.08.062, 2014.

Li, C., Hu, Y., Chen, J., Ma, Z., Ye, X., Yang, X., Wang, L., Wang, X., and Mellouki, A.: Physiochemical properties of carbonaceous aerosol from agricultural residue burning: Density, volatility, and hygroscopicity, Atmos. Environ., 140, 94-105, https://doi.org/10.1016/j.atmosenv.2016.05.052, 2016.

Li, G., Su, H., Ma, N., Tao, J., Kuang, Y., Wang, Q., Hong, J., Zhang, Y., Kuhn, U., Zhang, S., Pan, X., Lu, N., Tang, M., Zheng, G., Wang, Z., Gao, Y., Cheng, P., Xu, W., Zhou, G., Zhao, C., Yuan, B., Shao, M., Ding, A., Zhang, Q., Fu, P., Sun, Y., Poschl, U., and Cheng, Y.: Multiphase chemistry experiment in Fogs and Aerosols in the North China Plain (McFAN): integrated analysis and intensive winter campaign 2018, Faraday. Discuss., 226, 207-222, https://doi.org/10.1039/d0fd00099j, 2021a.

Li, J., Cao, L., Gao, W., He, L., Yan, Y., He, Y., Pan, Y., Ji, D., Liu, Z., and Wang, Y.: Seasonal variations in the highly time-resolved aerosol composition, sources and chemical processes of background submicron particles in the North China Plain, Atmos. Chem. Phys., 21, 4521-4539, https://doi.org/10.5194/acp-21-4521-2021, 2021b.

Lin, Y., Bahreini, R., Zimmerman, S., Fofie, E. A., Asa-Awuku, A., Park, K., Lee, S.-B., Bae, G.-N., and Jung, H. S.: Investigation of ambient aerosol effective density with and without using a catalytic stripper, Atmos. Environ., 187, 84-92, https://doi.org/10.1016/j.atmosenv.2018.05.063, 2018.

Ma, N., Zhao, C., Müller, T., Cheng, Y., Liu, P., Deng, Z., Xu, W., Ran, L., Nekat, B., Pinxteren, D. v., Gnauk, T., Mueller, K., Herrmann, H., Yan, P., Zhou, X., and Wiedensohler, A.: A new method to determine the mixing state of light absorbing carbonaceous using the measured aerosol optical properties and number size distributions, Atmos. Chem. Phys., 12, 2381-2397, https://doi.org/10.5194/acp-12-2381-2012, 2012.

Ma, Y., Li, S., Zheng, J., Khalizov, A., Wang, X., Wang, Z., and Zhou, Y.: Size-resolved measurements of mixing state and cloud-nucleating ability of aerosols in Nanjing, China, J. Geophys. Res. Atmos., 122, 9430-9450, https://doi.org/10.1002/2017JD026583, 2017.

Ma, Y., Huang, C., Jabbour, H., Zheng, Z., Wang, Y., Jiang, Y., Zhu, W., Ge, X., Collier, S., and Zheng, J.: Mixing state and light absorption enhancement of black carbon aerosols in summertime Nanjing, China, Atmos. Environ., 222, 117141, https://doi.org/10.1016/j.atmosenv.2019.117141, 2020.

Malloy, Q. G., Nakao, S., Qi, L., Austin, R., Stothers, C., Hagino, H., and Cocker III, D. R.: Real-time aerosol density determination utilizing a modified scanning mobility particle sizer—aerosol particle mass analyzer system, Aerosol. Sci. Tech., 43, 673-678, https://doi.org/10.1080/02786820902832960, 2009.

McMurry, P. H., Wang, X., Park, K., and Ehara, K.: The relationship between mass and mobility for atmospheric particles: A new technique for measuring particle density, Aerosol. Sci. Tech., 36, 227-238, https://doi.org/10.1080/027868202753504083, 2002.

Nakao, S., Shrivastava, M., Nguyen, A., Jung, H., and Cocker III, D.: Interpretation of secondary organic aerosol formation from diesel exhaust photooxidation in an environmental chamber, Aerosol. Sci. Tech., 45, 964-972, https://doi.org/10.1080/02786826.2011.573510, 2011.

Ng, N. L., Herndon, S. C., Trimborn, A., Canagaratna, M. R., Croteau, P., Onasch, T. B., Sueper, D., Worsnop, D. R., Zhang, Q., Sun, Y., and Jayne, J.: An Aerosol Chemical Speciation Monitor (ACSM) for routine monitoring of the composition and mass concentrations of ambient aerosol, Aerosol. Sci. Tech., 45, 780-794, https://doi.org/10.1080/02786826.2011.560211, 2011.

Nosko, O. and Olofsson, U.: Effective density of airborne wear particles from car brake materials, J. Aerosol. Sci., 107, 94-106, https://doi.org/10.1016/j.jaerosci.2017.02.014, 2017.

Olfert, J., Symonds, J., and Collings, N.: The effective density and fractal dimension of particles emitted from a light-duty diesel vehicle with a diesel oxidation catalyst, J. Aerosol. Sci., 38, 69-82, https://doi.org/10.1016/j.jaerosci.2006.10.002, 2007.

Olfert, J. S., Dickau, M., Momenimovahed, A., Saffaripour, M., Thomson, K., Smallwood, G., Stettler, M. E., Boies, A., Sevcenco, Y., and Crayford, A.: Effective density and volatility of particles sampled from a helicopter gas turbine engine, Aerosol. Sci. Tech., 51, 704-714, https://doi.org/10.1080/02786826.2017.1292346, 2017.

Olfert, J. and Rogak, S.: Universal relations between soot effective density and primary particle size for common combustion sources, Aerosol. Sci. Tech., 53, 485-492, https://doi.org/10.1080/02786826.2019.1577949, 2019.

Pagels, J., Khalizov, A. F., McMurry, P. H., and Zhang, R. Y.: Processing of soot by controlled sulphuric acid and water condensation—Mass and mobility relationship, Aerosol. Sci. Tech., 43, 629-640, https://doi.org/10.1080/02786820902810685, 2009.

Park, K., Cao, F., Kittelson, D. B., and McMurry, P. H.: Relationship between particle mass and mobility for diesel exhaust particles, Environ. Sci. Technol., 37, 577-583, https://doi.org/10.1021/es025960v, 2003.

Peng, J., Hu, M., Guo, S., Du, Z., Zheng, J., Shang, D., Zamora, M. L., Zeng, L., Shao, M., Wu, Y.-S., Zheng, J., Wang, Y., Glen, C., Collins, D., Molina, M., and Zhang, R.: Markedly enhanced absorption and direct radiative forcing of black carbon under polluted urban environments, P. Natl. Acad. Sci. USA., 113, 4266-4271, https://doi.org/10.1073/pnas.1602310113, 2016.

Peng, L., Li, Z., Zhang, G., Bi, X., Hu, W., Tang, M., Wang, X., and Sheng, G.: A review of measurement techniques for aerosol effective density, Sci. Total. Environ., 778, 146248, https://doi.org/10.1016/j.scitotenv.2021.146248, 2021.

Qiao, K., Wu, Z., Pei, X., Liu, Q., Shang, D., Zheng, J., Du, Z., Zhu, W., Wu, Y., Lou, S., Guo, S., Chan, C. K., Pathak, R. K., Hallquist, M., and Hu, M.: Size-resolved effective density of submicron particles during summertime in the rural atmosphere of Beijing, China, J. Environ. Sci., 73, 69-77, https://doi.org/10.1016/j.jes.2018.01.012, 2018.

Rissler, J., Messing, M. E., Malik, A. I., Nilsson, P. T., Nordin, E. Z., Bohgard, M., Sanati, M., and Pagels, J. H.: Effective density characterization of soot agglomerates from various sources and comparison to aggregation theory, Aerosol. Sci. Tech., 47, 792-805, https://doi.org/10.1080/02786826.2013.791381, 2013.

Rissler, J., Nordin, E. Z., Eriksson, A. C., Nilsson, P. T., Frosch, M., Sporre, M. K., Wierzbicka, A., Svenningsson, B., Löndahl, J., Messing, M. E., Sjogren, S., Hemmingsen, J. G., Loft, S., Pagels, J. H., and Swietlicki, E.: Effective density and mixing state of aerosol particles in a near-traffic urban environment, Environ. Sci. Technol., 48, 6300-6308, https://doi.org/10.1021/es5000353, 2014.

Schmid, O., Karg, E., Hagen, D. E., Whitefield, P. D., and Ferron, G. A.: On the effective density of non-spherical particles as derived from combined measurements of aerodynamic and mobility equivalent size, J. Aerosol. Sci., 38, 431-443, https://doi.org/10.1016/j.jaerosci.2007.01.002, 2007.

Spencer, M. T., Shields, L. G., and Prather, K. A.: Simultaneous measurement of the effective density and chemical composition of ambient aerosol particles, Environ. Sci. Technol., 41, 1303-1309, https://doi.org/10.1021/es061425+, 2007.

Su, H., Cheng, Y., and Poschl, U.: New multiphase chemical processes influencing atmospheric aerosols, air quality, and climate in the anthropocene, Accounts. Chem. Res., 53, 2034-2043, https://doi.org/10.1021/acs.accounts.0c00246, 2020.

Tavakoli, F. and Olfert, J. S.: Determination of particle mass, effective density, mass–mobility exponent, and dynamic shape factor using an aerodynamic aerosol classifier and a differential mobility analyzer in tandem, J. Aerosol. Sci., 75, 35-42, https://doi.org/10.1016/j.jaerosci.2014.04.010, 2014.

Turpin, B. J. and Lim, H.-J.: Species contributions to $PM_{2.5}$ mass concentrations: Revisiting common assumptions for estimating organic mass, Aerosol. Sci. Tech., 35, 602-610, https://doi.org/10.1080/02786820119445, 2001.

Ubogu, E. A., Cronly, J., Khandelwal, B., and Roy, S.: Determination of the effective density and fractal dimension of PM emissions from an aircraft auxiliary power unit, J. Environ. Sci., 74, 11-18, https://doi.org/10.1016/j.jes.2018.01.027, 2018.

Wang, M., Tang, Q., Mei, J., and You, X.: On the effective density of soot particles in premixed ethylene flames, Combust. Flame., 198, 428-435, https://doi.org/10.1016/j.combustflame.2018.10.004, 2018.

Wiedensohler, A.: An approximation of the bipolar charge distribution for particles in the submicron size range, J. Aerosol. Sci., 19, 387-389, https://doi.org/10.1016/0021-8502(88)90278-9, 1988.

Wu, Y., Xia, Y., Huang, R., Deng, Z., Tian, P., Xia, X., and Zhang, R.: A study of the morphology and effective density of externally mixed black carbon aerosols in ambient air using a size-resolved single-particle soot photometer (SP2), Atmos. Meas. Tech., 12, 4347-4359, https://doi.org/10.5194/amt-12-4347-2019, 2019.

Xie, Y., Ye, X., Ma, Z., Tao, Y., Wang, R., Zhang, C., Yang, X., Chen, J., and Chen, H.: Insight into winter haze formation mechanisms based on aerosol hygroscopicity and effective density measurements, Atmos. Chem. Phys., 17, 7277-7290, https://doi.org/10.5194/acp-17-7277-2017, 2017.

595 Yan, Y., Liu, Z., Gao, W., Li, J., Zhang, X., Chai, W., Bai, J., Hu, B., and Wang, Y.: Physiochemistry characteristics and sources of submicron aerosols at the background area of North China Plain: Implication of air pollution control in heating season, Atmos. Res., 249, 105291, https://doi.org/10.1016/j.atmosres.2020.105291, 2021.

Yang, F., Tan, J., Zhao, Q., Du, Z., He, K., Ma, Y., Duan, F., Chen, G., and Zhao, Q.: Characteristics of $PM_{2.5}$ speciation in representative megacities and across China, Atmos. Chem. Phys., 11, 5207-5219, https://doi.org/10.5194/acp-11-5207-2011,
600 2011.

Yin, Z., Ye, X., Jiang, S., Tao, Y., Shi, Y., Yang, X., and Chen, J.: Size-resolved effective density of urban aerosols in Shanghai, Atmos. Environ., 100, 133-140, https://doi.org/10.1016/j.atmosenv.2014.10.055, 2015.

Zamora, M. L., Peng, J., Hu, M., Guo, S., Marrero-Ortiz, W., Shang, D., Zheng, J., Du, Z., Wu, Z., and Zhang, R.: Wintertime aerosol properties in Beijing, Atmos. Chem. Phys., 19, 14329-14338, https://doi.org/10.5194/acp-19-14329-2019,
605 2019.

Zhai, J., Lu, X., Li, L., Zhang, Q., Zhang, C., Chen, H., Yang, X., and Chen, J.: Size-resolved chemical composition, effective density, and optical properties of biomass burning particles, Atmos. Chem. Phys., 17, 7481-7493, https://doi.org/10.5194/acp-17-7481-2017, 2017.

Zhang, R., Khalizov, A. F., Pagels, J., Zhang, D., Xue, H., and McMurry, P. H.: Variability in morphology, hygroscopicity,
610 and optical properties of soot aerosols during atmospheric processing, P. Natl. Acad. Sci. USA., 105, 10291-10296, https://doi.org/10.1073/pnas.0804860105, 2008.

Zhang, G., Bi, X., Qiu, N., Han, B., Lin, Q., Peng, L., Chen, D., Wang, X., Peng, P. a., Sheng, G., and Zhou, Z.: The real part of the refractive indices and effective densities for chemically segregated ambient aerosols in Guangzhou measured by a single-particle aerosol mass spectrometer, Atmos. Chem. Phys., 16, 2631-2640, https://doi.org/10.5194/acp-16-2631-2016,
615 2016a.

Zhang, Y., Zhang, Q., Cheng, Y., Su, H., Kecorius, S., Wang, Z., Wu, Z., Hu, M., Zhu, T., Wiedensohler, A., and He, K.: Measuring the morphology and density of internally mixed black carbon with SP2 and VTDMA: new insight into the absorption enhancement of black carbon in the atmosphere, Atmos. Meas. Tech., 9, 1833-1843, https://doi.org/10.5194/amt-9-1833-2016, 2016b.

620 Zhang, Y., Su, H., Ma, N., Li, G., Kecorius, S., Wang, Z., Hu, M., Zhu, T., He, K., Wiedensohler, A., Zhang, Q., and Cheng, Y.: Sizing of Ambient particles from a single-particle soot photometer measurement to retrieve mixing state of black carbon at a regional site of the North China Plain, J. Geophys. Res. Atmos., 123, https://doi.org/10.1029/2018JD028810, 2018.

https://doi.org/10.5194/acp-2021-463
Preprint. Discussion started: 22 June 2021

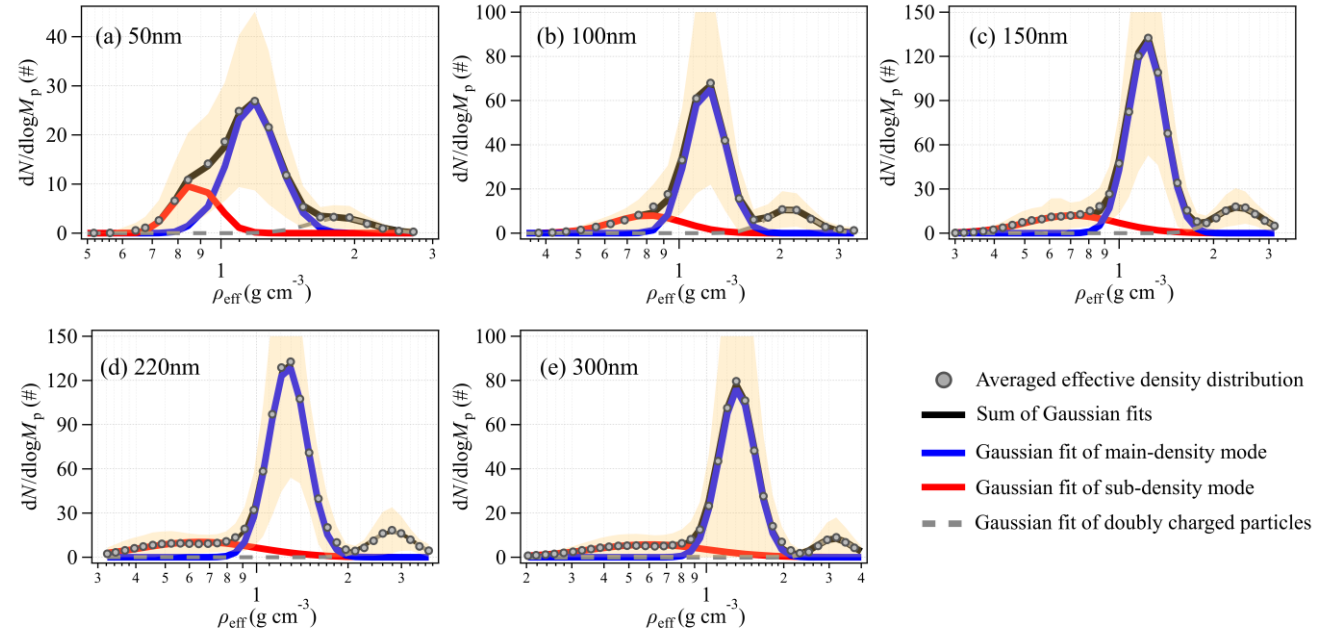

Figure 1: Averaged particle effective density (ρ_{eff}) distribution for (a) 50 nm, (b) 100 nm, (c) 150 nm, (d) 220 nm, and (e) 300 nm particles during the entire sampling period. The grey points represent the measured average effective density distribution, and yellow shadowed area represents the standard deviation of the averaged data. The blue and red line are Gaussian fit of the main-density and sub-density mode at each size, respectively, and the grey dashed line represents Gaussian fit of doubly charged particles. The black line is the sum of the main-density, sub-density mode and doubly charged particles.

https://doi.org/10.5194/acp-2021-463
Preprint. Discussion started: 22 June 2021

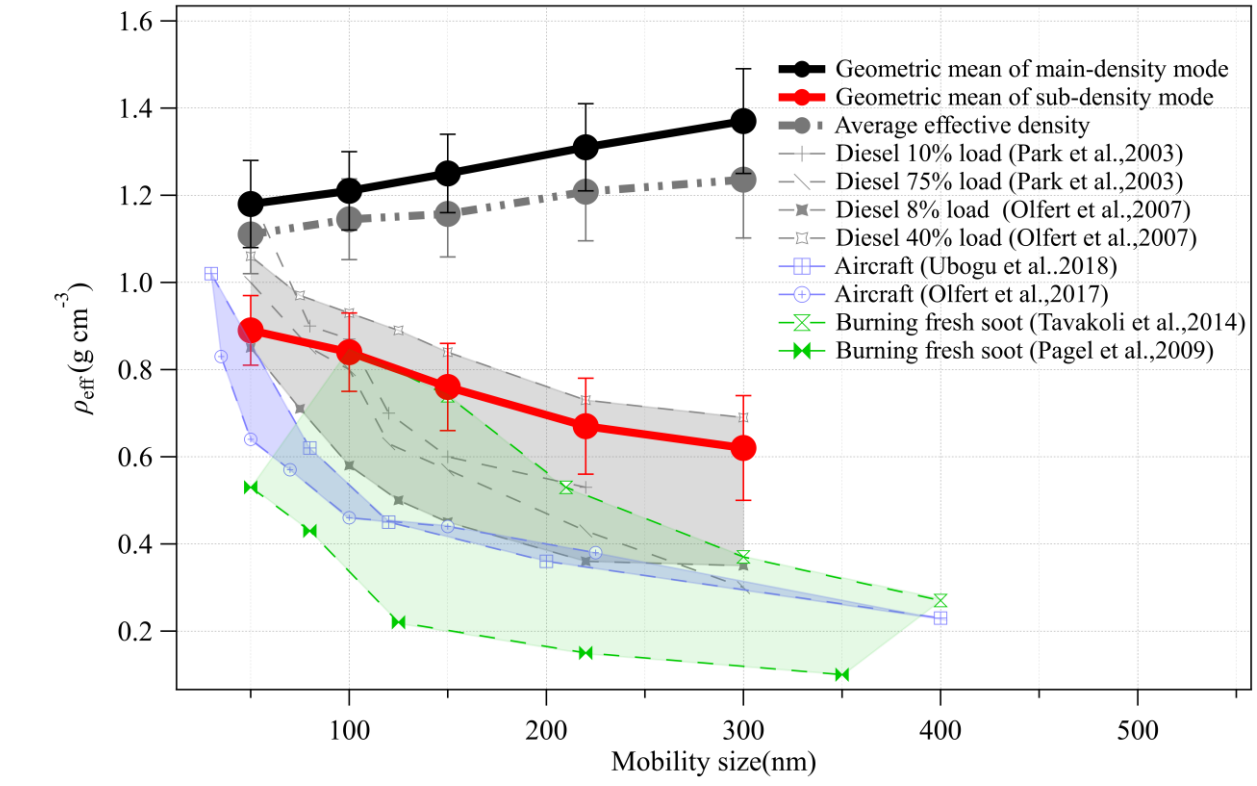

630 **Figure 2: Trend lines of effective density (ρ_{eff}) against mobility size and a summary of soot effective density from a wide range of primary emissions.**

https://doi.org/10.5194/acp-2021-463
Preprint. Discussion started: 22 June 2021

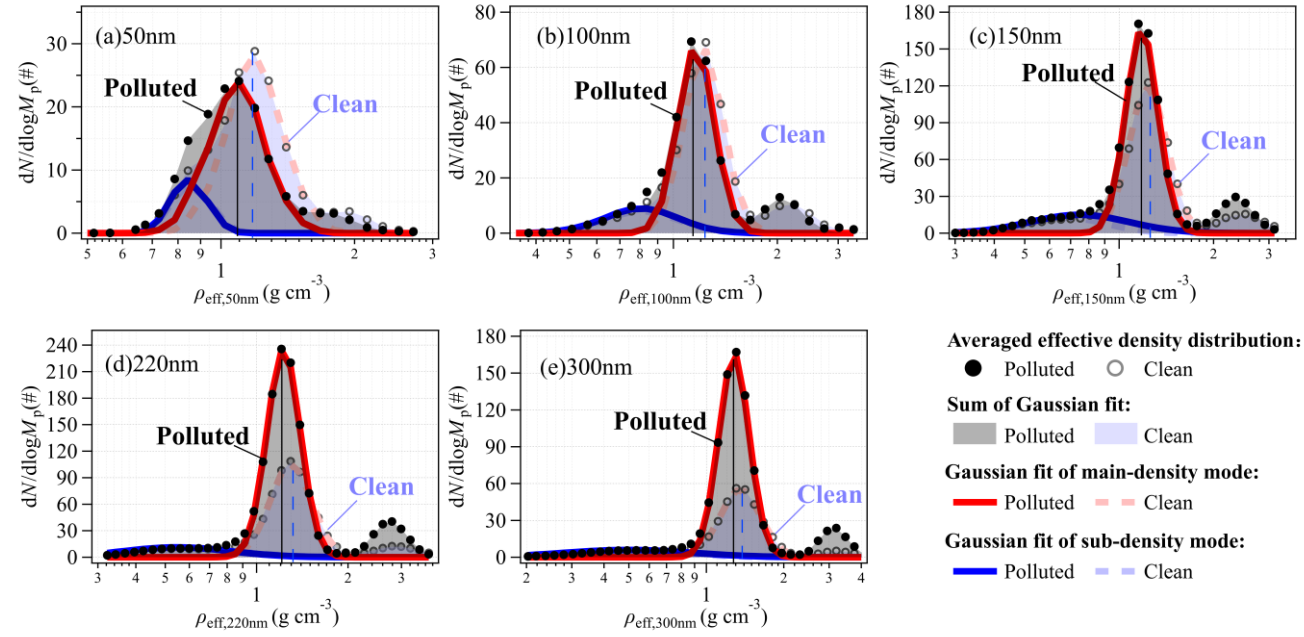

Figure 3: Averaged particle effective density (ρ_{eff}) distribution for (a) 50 nm, (b) 100 nm, (c) 150 nm, (d) 220 nm, and (e) 300 nm particles under polluted and clean conditions.

https://doi.org/10.5194/acp-2021-463
Preprint. Discussion started: 22 June 2021

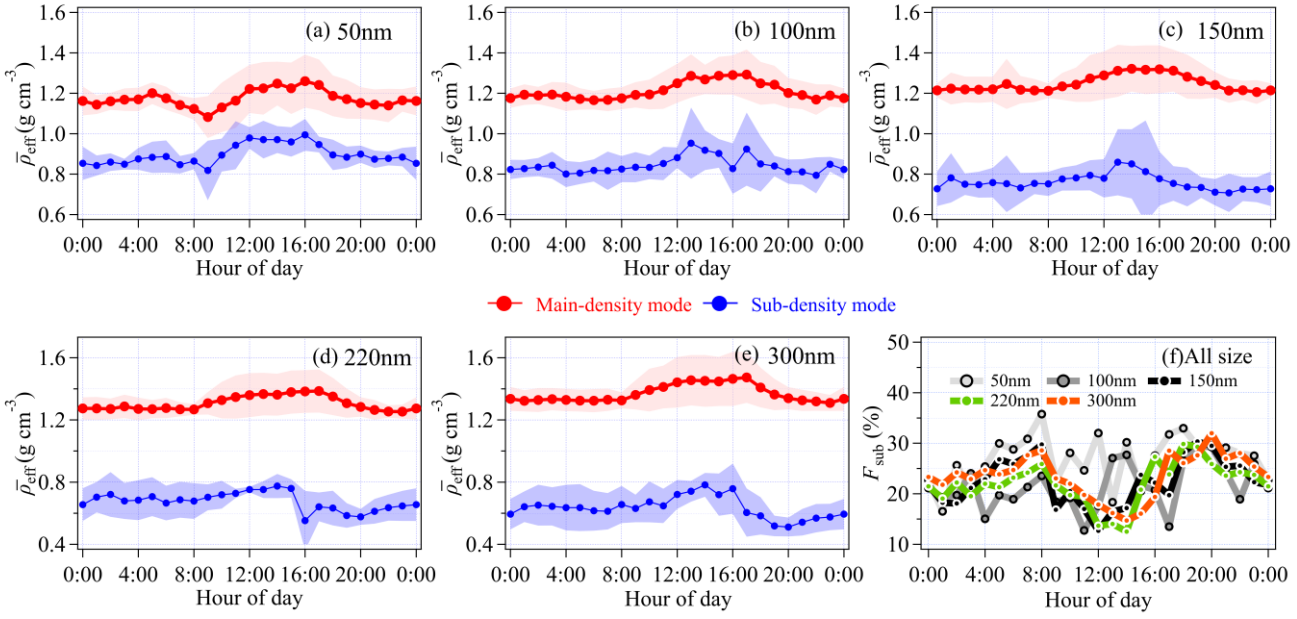

635

Figure 4: Diurnal cycle of: geometric mean effective density ($\overline{\rho}_{eff}$) of the main-density and sub-density mode for (a) 50 nm, (b) 100 nm, (c) 150 nm, (d) 220 nm, and (e) 300 nm particles; (f) number fraction of the sub-density mode (F_{sub}).

https://doi.org/10.5194/acp-2021-463
Preprint. Discussion started: 22 June 2021

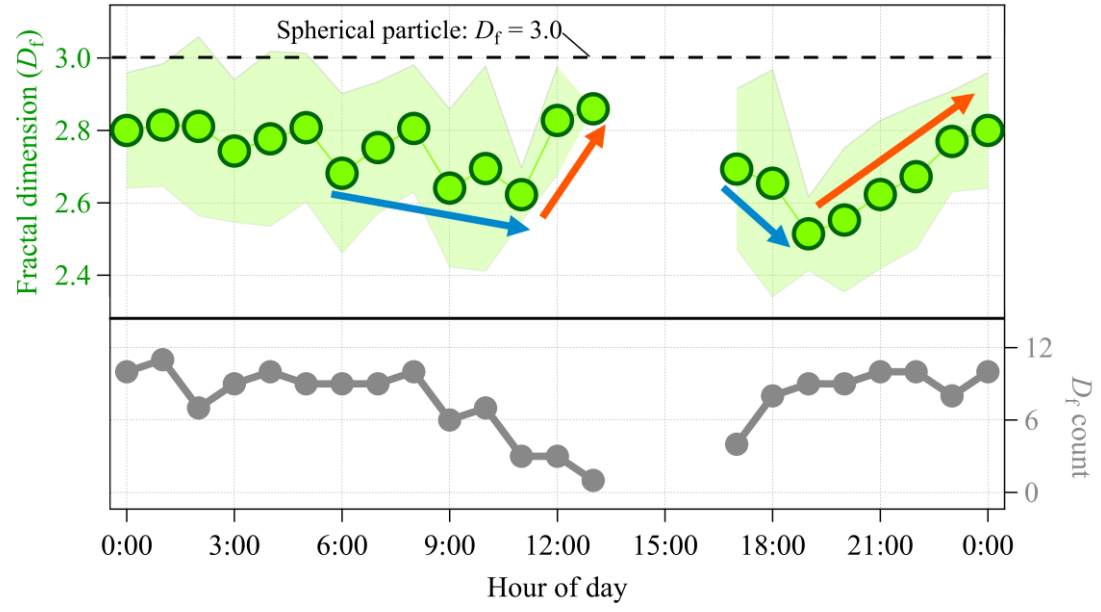

640 **Figure 5: Diurnal cycle of fractal dimension (D_f) of the sub-density mode particles. The dotted line is Df with the value of 3.0, indicating particle with a spherical morphology. The blue arrows represent D_f with decreasing trend and the orange arrows represent D_f with increasing trend.**

https://doi.org/10.5194/acp-2021-463
Preprint. Discussion started: 22 June 2021

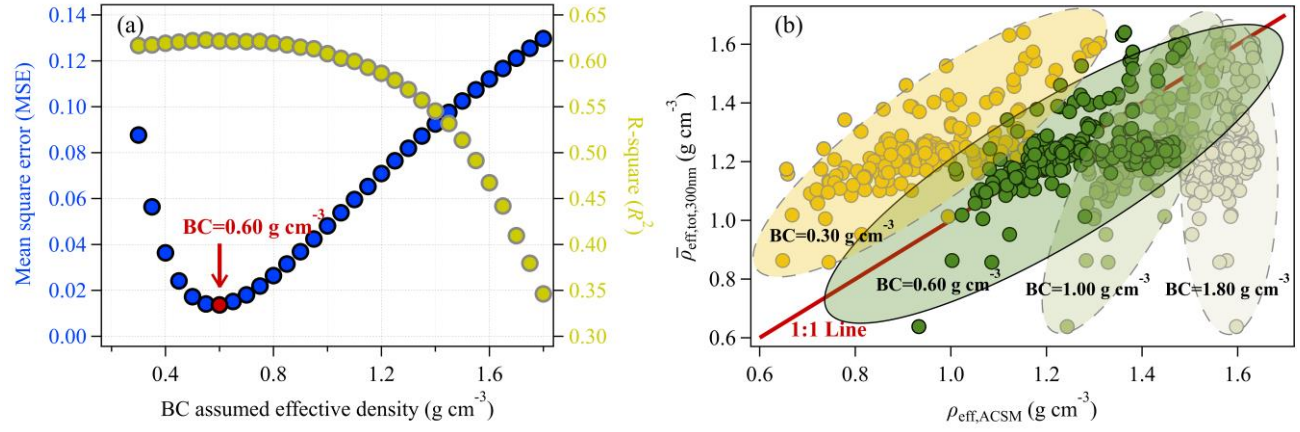

Figure 6: (a) Mean square error (MSE) and R-square (R^2) results from BC effective density sensitivity test. (b) Comparison of the average effective density of particles at 300 nm observed by DMA-CPMA-CPC ($\overline{\rho}_{eff,tot,300nm}$) and ACSM-derived bulk effective density ($\rho_{eff,ACSM}$). The color shaded areas represent $\rho_{eff,ACSM}$ based on different BC effective density assumption. Red line is the line with slope of 1.

https://doi.org/10.5194/acp-2021-463
Preprint. Discussion started: 22 June 2021

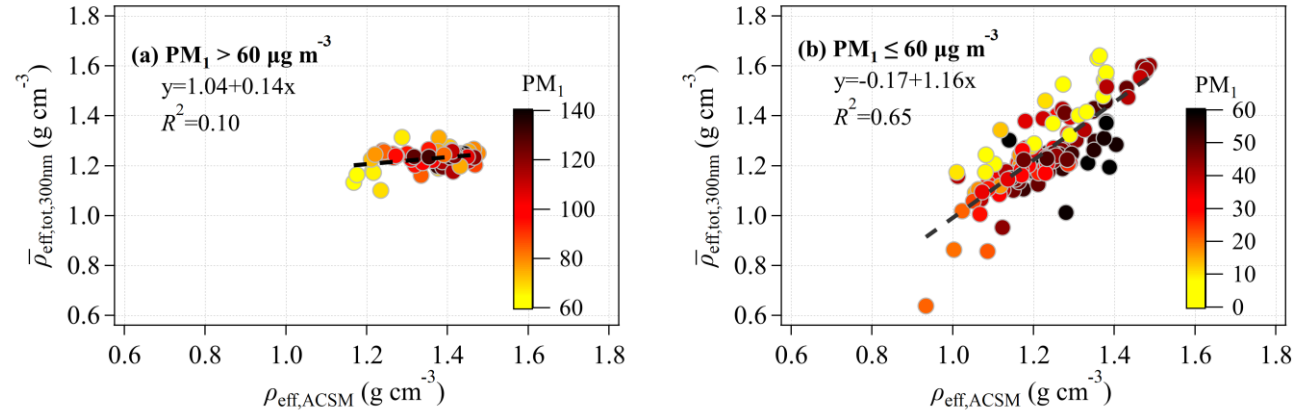

Figure 7: Comparison of the average effective density of particles at 300 nm observed by DMA-CPMA-CPC ($\overline{\rho}_{eff,tot,300nm}$) and ACSM-derived bulk effective density ($\rho_{eff,ACSM}$) under (a) polluted (corresponding to PM_1 > 60 µg m^{-3}) and (b) clean (corresponding to $PM_1 \leq 60$ µg m^{-3}) condition. Colored circles represent PM_1 mass concentrations.

https://doi.org/10.5194/acp-2021-463
Preprint. Discussion started: 22 June 2021

Atmospheric Chemistry and Physics Discussions

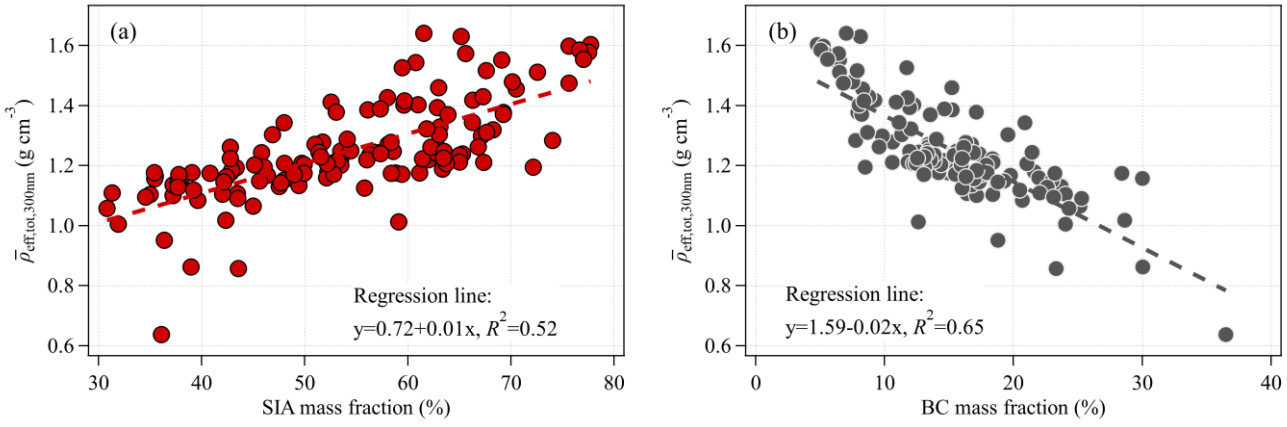

Figure 8: Correlation between (a) SIA, (b) BC mass fraction and $\overline{\rho}_{eff,tot,300nm}$ under clean condition.

https://doi.org/10.5194/acp-2021-463
Preprint. Discussion started: 22 June 2021

Atmospheric Chemistry and Physics Discussions

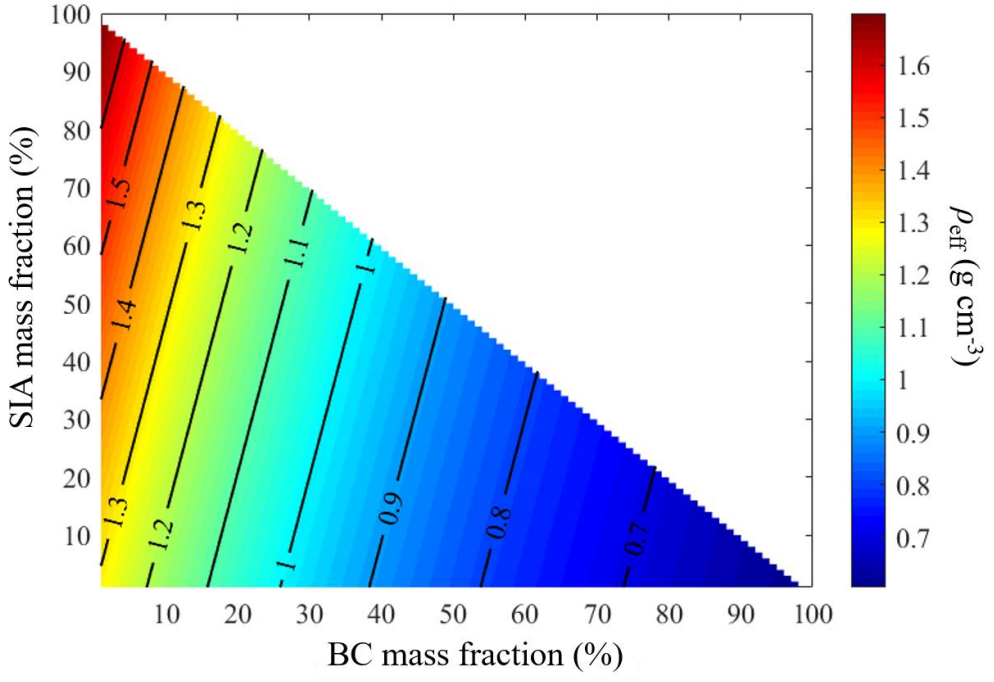

Figure 9: Particle effective density (ρ_{eff}) calculation based on assumed chemical composition.

https://doi.org/10.5194/acp-2021-463
Preprint. Discussion started: 22 June 2021

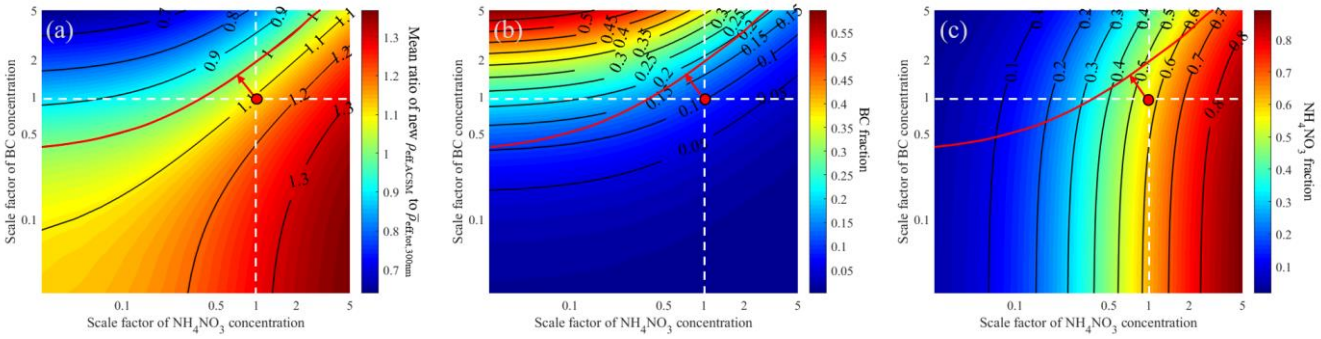

Figure 10: (a) Mean ratio of new calculated $\rho_{eff,ACSM}$ versus measured $\bar{\rho}_{eff,tot,300nm}$ based on scale factor of NH_4NO_3 and BC mass concentrations ranging from 0.01 to 5 (at logarithmic scale), (b) the corresponding NH_4NO_3 mass fraction and (c) the corresponding BC mass fraction under polluted condition. The black lines represent contours with the same values. The vertical and horizonal white dotted lines respectively represent NH_4NO_3 and BC mass concentration at the scale factor of 1, and red circles are original mass concentrations of BC and NH_4NO_3.

https://doi.org/10.5194/acp-2021-463
Preprint. Discussion started: 22 June 2021

Atmospheric Chemistry and Physics Discussions

Table 1: The geometric mean effective density ($\bar{\rho}_{\mathbf{eff,sub}}$ and $\bar{\rho}_{\mathbf{eff,main}}$) and standard deviation ($\sigma_{\mathbf{sub}}$ and $\sigma_{\mathbf{main}}$) of the sub-density and main-density mode, number fraction ($F_{\mathbf{sub}}$) and occurrence frequency of the sub-density mode during the entire sampling period

Size(nm)	$\bar{\rho}_{\mathrm{eff,sub}}$(g cm^{-3})	$\bar{\rho}_{\mathrm{eff,main}}$(g cm^{-3})	σ_{main}	σ_{sub}	F_{sub}(%)	Frequency(%)
50	0.89±0.08	1.18±0.10	0.053±0.012	0.044±0.014	27±18	79
100	0.84±0.09	1.21±0.09	0.051±0.010	0.074±0.027	22±11	87
150	0.76±0.10	1.25±0.09	0.053±0.007	0.129±0.034	23±12	86
220	0.67±0.11	1.31±0.10	0.059±0.008	0.172±0.037	23±10	77
300	0.62±0.12	1.37±0.12	0.067±0.010	0.215±0.036	25±10	81

https://doi.org/10.5194/acp-2021-463
Preprint. Discussion started: 22 June 2021

Atmospheric Chemistry and Physics Discussions

Table 2: The geometric mean effective density ($\bar{\rho}_{\mathrm{eff,sub}}$ and $\bar{\rho}_{\mathrm{eff,main}}$) of the sub-density and main-density mode, number fraction (F_{sub}) and occurrence frequency of the sub-density mode under polluted and clean conditions.

Size(nm)	Condition	$\bar{\rho}_{\mathrm{eff,sub}}$(g cm^{-3})	$\bar{\rho}_{\mathrm{eff,main}}$(g cm^{-3})	F_{sub}(%)	Frequency(%)
50	Polluted	0.87±0.06	1.11±0.09	42±25	72
	Clean	0.90±0.08	1.19±0.10	24±13	81
100	Polluted	0.83±0.07	1.15±0.05	25±11	95
	Clean	0.84±0.09	1.23±0.09	21±11	84
150	Polluted	0.74±0.05	1.18±0.04	20±8	89
	Clean	0.76±0.10	1.27±0.09	24±12	86
220	Polluted	0.68±0.10	1.23±0.03	18±3	63
	Clean	0.67±0.11	1.33±0.11	24±11	82
300	Polluted	0.65±0.13	1.29±0.03	18±4	57
	Clean	0.62±0.12	1.40±0.12	26±11	89